

# Topological-chiral magnetic interactions in ultrathin films at surfaces

Soumyajyoti Haldar,<sup>1,\*</sup> Sebastian Meyer,<sup>1,†</sup> André Kubetzka,<sup>2</sup> and Stefan Heinze<sup>1</sup>

<sup>1</sup>*Institute of Theoretical Physics and Astrophysics, University of Kiel, Leibnizstrasse 15, 24098 Kiel, Germany*

<sup>2</sup>*Department of Physics, University of Hamburg, 20355 Hamburg, Germany*

(Dated: June 17, 2021)

We demonstrate that topological-chiral magnetic interactions can play a key role for magnetic ground states in ultrathin films at surfaces. Based on density functional theory we show that significant chiral-chiral interactions occur in hexagonal Mn monolayers due to large topological orbital moments which interact with the emergent magnetic field. Due to the competition with higher-order exchange interactions superposition states of spin spirals such as the 2Q state or a distorted 3Q state arise. Simulations of spin-polarized scanning tunneling microscopy images suggest that the distorted 3Q state could be the magnetic ground state of a Mn monolayer on Re(0001).

Non-collinear spin structures are of fundamental interest in magnetism since they allow to obtain insight into the underlying microscopic interactions and are promising for spintronic applications [1, 2]. For example, the frustration of Heisenberg exchange interactions is the origin of spin spiral states found in many rare-earth elements or in the fcc-phase of Fe. The competition with beyond nearest-neighbor exchange occurs due to the long-range nature of the RKKY interaction characteristic for transition and rare-earth metals. Spin spirals can also arise due to the Dzyaloshinskii-Moriya (DM) interaction which occurs in materials with broken inversion symmetry such as surfaces or interfaces [3].

Recently, more complex magnetic states such as the superposition of spin spirals [4–6] or atomic scale spin lattices [7–9] have raised much attention. They can occur due to terms beyond the pair-wise Heisenberg or DM interactions such as higher-order exchange interactions [10–12]. They might also be driven by the recently proposed topological-chiral [13] and chiral multi-spin interactions [14–16]. A prominent example of a multi-Q state – a superposition of symmetry equivalent spin spirals (1Q states) – is the 3Q state [4]. The 3Q state, which has first been predicted as the ground state of a Mn monolayer on Cu(111) [4], is an intriguing non-collinear spin structure on a two-dimensional lattice which leads to topological orbital moments and a topological Hall effect even in the absence of spin-orbit coupling [17]. It has also been predicted to trigger topological superconductivity in a conventional superconductor [18]. Recently, the 3Q state has been discovered in a Mn monolayer on the Re(0001) surface by spin-polarized scanning tunneling microscopy (SP-STM) [6]. However, the locking of the spin structure to the atomic lattice could not be explained and it was speculated that a distortion of the 3Q state could be the origin.

Here we demonstrate based on density functional theory (DFT) that the recently discovered topological-chiral magnetic interactions [13] can be essential for the magnetic ground state of ultrathin films at surfaces. For free-standing Mn monolayers we show that large topological

orbital moments occur which interact with the emerging magnetic field leading to significant chiral-chiral interactions. By the interplay of this term with higher-order exchange interactions complex spin structures such as the 2Q state or the distorted 3Q state can be stabilized. For Mn monolayers on Cu(111) and Re(0001) we predict similarly large chiral-chiral interactions which could induce a distorted 3Q state magnetic ground state for Mn/Re(0001). By simulating scanning tunneling microscopy images we show how the predicted magnetic ground states and thus the topological-chiral magnetic interactions may be verified experimentally.

We have used DFT as implemented in the FLEUR code [19] which is based on the full-potential linearized augmented plane wave (FLAPW) method [20] to calculate total energies of non-collinear spin structures [21] for unsupported Mn monolayers and on the Re(0001) surface. The Mn monolayer has been studied in hcp stacking on Re(0001) using asymmetric films with 6 layers of Re. The films have been structurally relaxed as described in Ref. [6]. We have also used the VASP code [22] which is based on the projector augmented wave (PAW) method [23–25]. In these calculations we have also used asymmetric films for Mn/Re(0001) but have increased the Re substrate to 10 layers. In addition, we have studied Mn/Cu(111) via VASP. Calculations have been performed within the local density approximation (LDA) and in the scalar-relativistic approximation, i.e. neglecting spin-orbit coupling. Further computational details can be found in the supplemental material [26].

For unsupported Mn monolayers we have calculated the energy dispersion of spin spirals since they are the fundamental solution of the classical Heisenberg model. Spin spirals can be characterized by a vector  $\mathbf{q}$  from the Brillouin zone (BZ). The calculated energy dispersion is qualitatively the same for all considered Mn monolayers (see supplemental material [26]). Among all spin spiral states the row-wise antiferromagnetic (RW-AFM) state (Fig. 1(h)) is the energetically lowest. The RW-AFM state can propagate along one of the three symmetry equivalent directions of the surface corresponding to the

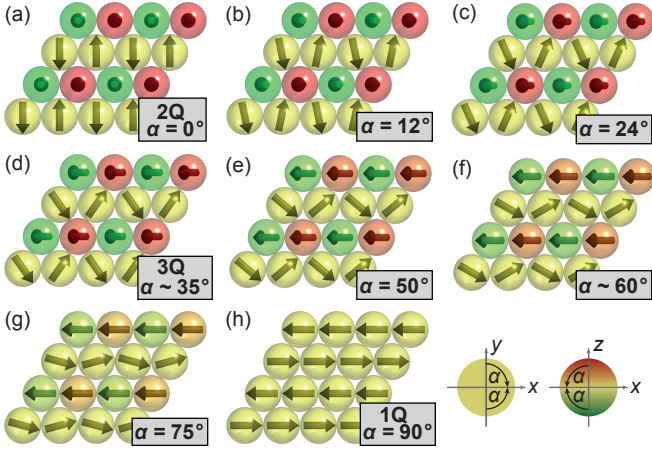


FIG. 1. Spin structures for a hexagonal Mn monolayer along the continuous path given by Eq. (1) from (a) the 2Q state via (d) the 3Q to (h) the 1Q state. Yellow arrows denote magnetic moments which rotate in the  $xy$  plane (shown in the coordinate system above), red arrows denote moments in the positive  $z$  direction, green arrows in the negative  $z$  direction. The angle  $\alpha$  is applied to rotate  $\pm z$  spins into the  $-x$  direction and  $\pm y$  spins to the  $+x$  direction. (a) 2Q state with  $\alpha = 0^\circ$ , (b)  $\alpha = 12^\circ$ , (c)  $\alpha = 24^\circ$ , (d) 3Q state with  $\alpha \sim 35^\circ$ , (e)  $\alpha = 50^\circ$ , (f)  $\alpha \sim 60^\circ$ , (g)  $\alpha = 75^\circ$ , (h) 1Q state (RW-AFM) with  $\alpha = 90^\circ$ .

$\bar{M}$  points of the two-dimensional BZ, i.e. 1Q states. One can construct linear combinations of two or three of these degenerate 1Q states under the constraint of fixed spin length at every lattice site resulting in the 2Q (Fig. 1(a)) and the 3Q (Fig. 1(d)) state, respectively. These states are energetically degenerate with the 1Q states within the classical Heisenberg model.

Figure 1 shows the spin structures which we consider in our total energy calculations to check for magnetic interactions beyond Heisenberg exchange. We start from the 2Q state, Fig. 1(a), and rotate all spins in this structure continuously into the 1Q (RW-AFM) state, Fig. 1(h). This is achieved based on the Rodriguez rotation formula such that the spin,  $\mathbf{s}_i^\nu$ , at site  $i$  in the  $\nu$ -th rotation step is given by (see supplemental material for details [26]):

$$\mathbf{s}_i^\nu = \mathbf{s}_i^{2Q} \cos \alpha_\nu + \mathbf{s}_i^{1Q} \sin \alpha_\nu, \quad (1)$$

where  $\mathbf{s}_i^{2Q}$  and  $\mathbf{s}_i^{1Q}$  are the spin directions in the 2Q and 1Q state, respectively. The rotation angle  $\alpha_\nu$  is varied from zero to  $90^\circ$ . The 3Q state corresponds to  $\alpha_\nu \approx 35^\circ$ , Fig. 1(d). It can be demonstrated that pair-wise Heisenberg exchange terms,  $-J_{ij}(\mathbf{s}_i \cdot \mathbf{s}_j)$ , where  $J_{ij}$  are the exchange constants, do not vary along this path (see Supplemental Material [26]). Therefore, any change of the total energy obtained via DFT can only be explained by terms beyond the Heisenberg exchange.

Figure 2(a) shows the total DFT energies obtained for the path defined by Eq. (1) via the FLEUR code for a hexagonal unsupported monolayer (UML) of Mn with different in-plane lattice constants, i.e. distance between

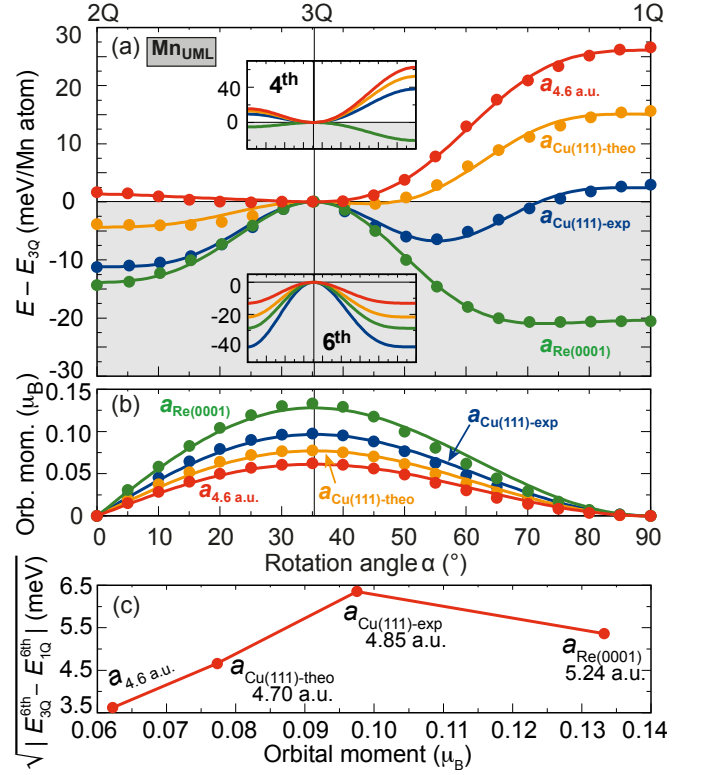


FIG. 2. (a) Energy along the 2Q-3Q-1Q path given by Eq. (1) in hexagonal Mn unsupported monolayers (UMLs) for different in-plane lattice constants. Symbols denote total energies calculated from DFT using the FLEUR code, the lines show the fit to higher-order-exchange interaction terms. The two insets show the contribution of the 4th and 6th order terms to the fit. Red color shows the result for  $a = 4.6$  a.u., orange and blue color for the theoretical and experimental in-plane lattice constant of Cu(111), respectively, and green color the values for the theoretical in-plane lattice constant of Re(0001) [27]. (b) Absolute value of the orbital moment per Mn atom along the direction perpendicular to the Mn UML. Symbols denote DFT values and lines the fit to the scalar spin chirality (see text for details). (c) Orbital moment of the 3Q state vs. the absolute value of the 6th-order energy contributions at the 1Q w.r.t to the 3Q state (cf. lower inset of Fig. 2(a)).

nearest-neighbor atoms. For the Mn UML on the lattice constant of  $a = 4.6$  a.u., we find that the 3Q state is the energetically lowest spin configuration. If we slightly increase the lattice constant to the value of the theoretical Cu lattice constant, the 2Q state shifts below the 3Q state. In addition, a small local energy minimum occurs close to the 3Q state. If the lattice constant is increased further to the experimental value of Cu the energy minimum of the distorted 3Q state (Fig. 1(f)) becomes more pronounced but the 2Q state remains the lowest state. For the even larger Re lattice constant the energy of the 1Q state has moved below the 2Q state. There is a tiny energy minimum for a distorted 1Q state with an angle of  $\alpha \approx 75^\circ$  (Fig. 1(g)).

The higher-order exchange interactions (HOI) of fourth order are the biquadratic interaction and the

three-site and four-site four spin interactions [12]:

$$H_{4th} = - \sum_{i,j} B_{ij} (\mathbf{s}_i \cdot \mathbf{s}_j)^2 - \sum_{ijk} Y_{ijk} [(\mathbf{s}_i \cdot \mathbf{s}_j)(\mathbf{s}_j \cdot \mathbf{s}_k) + (\mathbf{s}_j \cdot \mathbf{s}_i)(\mathbf{s}_i \cdot \mathbf{s}_k) + (\mathbf{s}_i \cdot \mathbf{s}_k)(\mathbf{s}_k \cdot \mathbf{s}_j)] + \sum_{ijkl} K_{ijkl} [(\mathbf{s}_i \cdot \mathbf{s}_j)(\mathbf{s}_k \cdot \mathbf{s}_l) + (\mathbf{s}_i \cdot \mathbf{s}_l)(\mathbf{s}_j \cdot \mathbf{s}_k) - (\mathbf{s}_i \cdot \mathbf{s}_k)(\mathbf{s}_j \cdot \mathbf{s}_l)], \quad (2)$$

where  $B_{ij}$ ,  $Y_{ijk}$  and  $K_{ijkl}$  are the corresponding higher-order exchange constants.

The energy of these three terms varies along the given path according to the function  $E_{4th}(\alpha) = \kappa_{4th}(2\cos^4\alpha + 6\sin^4\alpha - 4\cos^2\alpha\sin^2\alpha)$  with a strength  $\kappa_{4th}$  (see Supplemental Material [26]). This function has local extrema at the 1Q, 2Q, and 3Q state (see upper inset of Fig. 2(a)). Since the 2Q state is always in between the 1Q and the 3Q state, i.e. it cannot be the lowest state as long as higher-order terms are restricted to fourth order, it has been excluded in previous DFT calculations for Mn UMLs and Mn/Cu(111) [4]. However, the total energy calculations for Mn UML (Fig. 2(a)) cannot be explained based on the higher-order interactions given by Eq. (2). Note that the DFT calculations were performed in the scalar-relativistic approximation such that chiral-multi spin interactions [14–16] cannot occur.

Recently, it has been demonstrated that due to the interaction of the topological orbital moment, which can arise in non-collinear spin structures even in the absence of spin-orbit coupling [8, 17], with the emergent magnetic field the so-called chiral-chiral interaction occurs [13]:

$$H_{CC} = - \sum_{ijk} \kappa_{ijk}^{CC} [\mathbf{s}_i \cdot (\mathbf{s}_j \times \mathbf{s}_k)]^2 \quad (3)$$

with a site-dependent interaction strength  $\kappa_{ijk}^{CC}$ . This 6th order interaction scales with the square of the scalar spin chirality  $\chi_{ijk} = \mathbf{s}_i \cdot (\mathbf{s}_j \times \mathbf{s}_k)$  which varies for the given path at every site as  $\chi_{ijk} \propto \cos^2\alpha \sin\alpha$  (see Supplemental Material [26]). Therefore, the chiral-chiral interaction is proportional to  $\cos^4\alpha \sin^2\alpha$  (lower inset of Fig. 2(a)).

In order to check the importance of this interaction in our Mn UMLs we have calculated via DFT the topological orbital moment, which is proportional to the scalar spin chirality (Fig. 2(b)). As expected it exhibits a maximum at the 3Q state and vanishing values for the 2Q and 1Q state and is oriented perpendicular to the film. The orbital moment for the 3Q state is in good agreement with previous calculations [17]. An excellent fit is achieved for the angle dependent variation of the orbital moment (Fig. 2(b)) by using the analytical form of the scalar spin chirality given above.

The competition of 4th- and 6th-order interactions can explain the observed trend of the DFT energy curves for the Mn UMLs as shown by the insets of Fig. 2(a). The 4th-order contribution favors the 3Q state for the three lower lattice constants and the 1Q state for the Re lattice

constant. The 6th-order interaction, on the other hand, favors the 1Q and the 2Q state and drives the transition to the distorted 3Q state.

The trend of DFT curves in Fig. 2(a) is captured by considering only the 4th- and 6th-order term (see supplemental material [26]). To improve the fit, we added contributions from 8th- and 10th-order terms in Fig. 2(a). Such an expansion of a spin model for itinerant magnets in a power series of cosines between spins has been proposed [28] starting from the Liechtenstein formula [29].

To show the significance of the chiral-chiral interaction, we take a closer look to the 6th-order term (lower inset of Fig. 2(a)). The energy difference between the 3Q and the 1Q state of the 6th-order term increases proportional to the square of the topological orbital moment from  $a = 4.6$  a.u. up to  $a = 4.85$  a.u. (Fig. 2(c)). This is expected since the chiral-chiral interaction is proportional to the square of the scalar spin chirality while the orbital moment is linear with this quantity. At the Re lattice constant,  $a = 5.24$  a.u., the orbital moment further increases, while the energy contribution from the 6th order term decreases. Due to the large increase of the lattice constant the local density of states changes significantly (see supplemental material [26]) and thereby  $\kappa_{ijk}^{CC}$ , which depends on the electronic structure.

Note, that the bicubic interaction,  $(\mathbf{s}_i \cdot \mathbf{s}_j)^3$ , which is possible in systems with a spin moment of  $\geq 3\mu_B$  [12], could also contribute to the 6th order energy term since it exhibits the same functional form along the given path (see supplemental material [26]). However, the large topological orbital moments and the scaling of the 6th-order energy with the orbital moment provide strong evidence that the chiral-chiral interaction is dominating.

Now we turn to Mn monolayers on surfaces. The 3Q state has first been predicted for Mn/Cu(111) [4], however, the 2Q state had not been considered in that study. The DFT total energy curve along the path of Eq. (1) (Fig. 3(a)), obtained via VASP, is consistent with the expectation of Ref. [4], i.e. the 3Q state is lowest and the 2Q state lies between the 3Q and the 1Q state. However, a good fit of this energy curve requires to take not only the 4th order exchange interactions into account but also the 6th order terms (inset of Fig. 3(a)). The topological orbital moments are of the same order of magnitude as for the UMLs and can be fit by the scalar spin chirality (Fig. 3(c)). This shows that the chiral-chiral interaction is significant in this system.

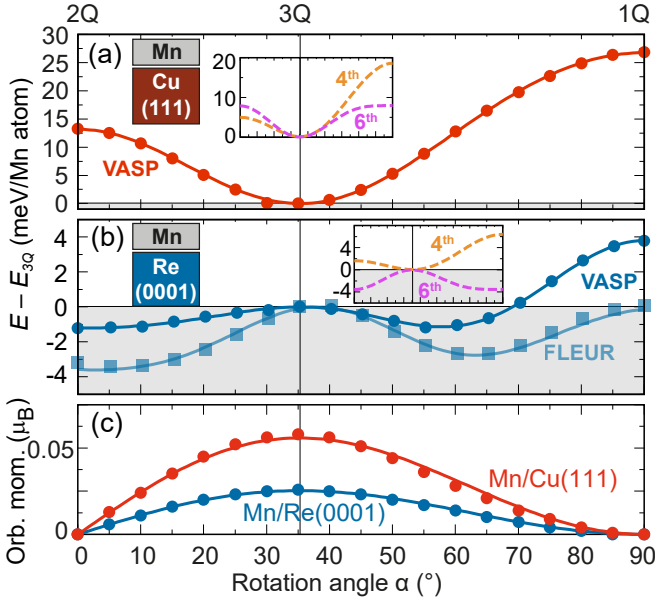


FIG. 3. Energy along the continuous 2Q-3Q-1Q path given by Eq. (1) in (a) Mn/Cu(111) and (b) Mn/Re(0001). Filled circles are energies calculated from DFT, the lines show the fit to higher-order-exchange interaction (insets show 4th and 6th order terms). For Mn/Cu(111) DFT calculations were performed using the VASP code and for Mn/Re(0001) both the FLEUR (squares) and the VASP code (circles) were applied. (c) Absolute value of the orbital moment per Mn atom directed perpendicular to the surface. Symbols denote DFT values and lines the fit to the scalar spin chirality.

Experimentally, the 3Q state was discovered in hcp-Mn/Re(0001) [6]. From previous DFT calculations it is known that the RW-AFM state (1Q state) is energetically lowest among all spin spiral states [6]. The 3Q state formed from a superposition of the three equivalent RW-AFM states [4] is even slightly lower in total energy. Surprisingly, the perfect 3Q state is only a local energy maximum along the path given by Eq. (1) while there are two local energy minima: one at the 2Q state and one for a distorted 3Q state (Fig. 3(b)). In the FLEUR calculation the 2Q state is slightly lower in energy and in VASP the two states are energetically nearly degenerate.

Similar to the case of the UMLs a good fit of the energy curve of Mn/Re(0001) can only be obtained if higher-order terms beyond fourth order are taken into account (inset of Fig. 3(b)). In particular, the 6th order terms, corresponding to the topological-chiral or bicubic interaction, are decisive to capture the two local energy minima. The topological orbital moments are smaller for Mn/Re(0001) (Fig. 3(c)) than for Mn/Cu(111) and so is the 6th order energy contribution.

Complex non-collinear spin structures in ultrathin films as proposed in this work can be resolved down to the atomic scale using SP-STM [30–32]. In order to check whether the three magnetic states compared above can be distinguished in an experiment, we have simulated

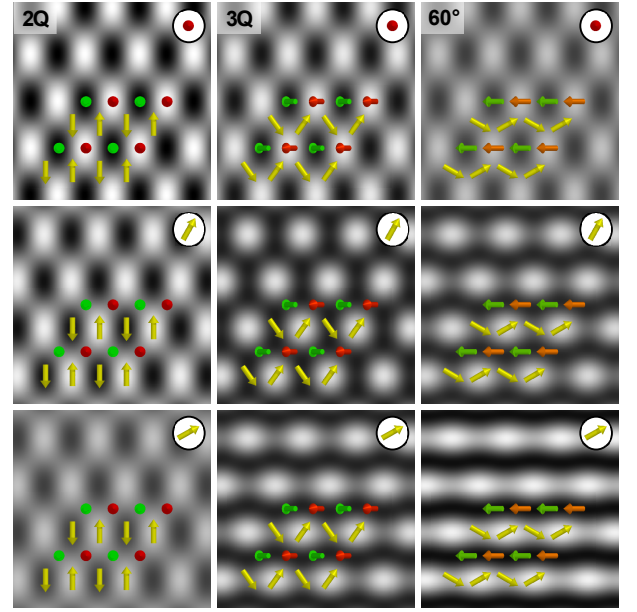


FIG. 4. Simulated spin-polarized scanning tunneling microscopy images at constant height (0.8 nm) for the 2Q, the 3Q, and the canted 3Q (60°) spin state for 3 different tip magnetization directions. The simulations have been performed using the model described in Ref. [30]. All panels have the same color scale of 1.5 pm from black to white.

SP-STM images for the 2Q state, the 3Q state, and the distorted 3Q state for three different magnetization directions of the STM tip (Fig. 4). For the 2Q state the contrast is very similar for the three cases which indicates that different rotational domains will look the same. For the 3Q state, in contrast, the SP-STM image for an out-of-plane magnetized tip (middle panel in the upper row of Fig. 4) is qualitatively different from that for a tip with an in-plane magnetization component (lower two panels in the middle row). Thereby, the 2Q and the 3Q state can be clearly distinguished if different rotational domains are imaged or if the tip magnetization is rotated by an external magnetic field.

In contrast, the SP-STM images of the distorted 3Q state are very similar to those of the ideal 3Q state and much harder to distinguish experimentally. However, the perfect 3Q state exhibits only a very weak coupling to the atomic lattice and the energetically preferred rotation of the 3Q state is in contrast to SP-STM experiments for Mn/Re(0001) [6]. Therefore, it has been proposed that a distorted 3Q state – such as the one found here – may explain the experimental observation since its reduced symmetry enhances the coupling to the atomic lattice.

In conclusion, we have demonstrated that the competition between higher-order exchange interactions and topological-chiral interactions needs to be taken into account in Mn monolayers. The novel types of magnetic ground states such as the 2Q or the distorted 3Q state will affect the transport properties of such systems [17] as well as their coupling to adjacent superconductors [18].



We anticipate that topological-chiral magnetic interactions play an important role for other film systems.

We gratefully acknowledge computing time at the supercomputer of the North-German Supercomputing Alliance (HLRN) and financial support from the Deutsche Forschungsgemeinschaft (DFG) via Project No. 418425860 and No. 408119516. It is our pleasure to thank Yuriy Mokrousov, Kirsten von Bergmann, Lydia Stühmer-Herrmann, Moritz Goerzen, Mara Gutzeit, and Souvik Paul for valuable discussions.

---

\* These two authors contributed equally; Email: [haldar@physik.uni-kiel.de](mailto:haldar@physik.uni-kiel.de)

† These two authors contributed equally; Current address: Nanomat/Q-mat/CESAM, Université de Liège, B-4000 Sart Tilman, Belgium

- [1] A. Fert, N. Reyren, and V. Cros, Magnetic skyrmions: advances in physics and potential applications, *Nat. Rev. Mater.* **2**, 17031 (2017).
- [2] J. Grollier, D. Querlioz, K. Camsari, and M. D. Stiles, Neuromorphic spintronics, *Nat. Electron.* **3**, 360 (2020).
- [3] M. Bode, M. Heide, K. von Bergmann, P. Ferriani, S. Heinze, G. Bihlmayer, A. Kubetzka, O. Pietzsch, S. Blügel, and R. Wiesendanger, Chiral magnetic order at surfaces driven by inversion asymmetry, *Nature* **447**, 190 (2007).
- [4] P. Kurz, G. Bihlmayer, K. Hirai, and S. Blügel, Three-Dimensional Spin Structure on a Two-Dimensional Lattice: Mn /Cu(111), *Phys. Rev. Lett.* **86**, 1106 (2001).
- [5] S. Hayami, R. Ozawa, and Y. Motome, Effective bilinear-biquadratic model for noncoplanar ordering in itinerant magnets, *Phys. Rev. B* **95**, 224424 (2017).
- [6] J. Spethmann, S. Meyer, K. von Bergmann, R. Wiesendanger, S. Heinze, and A. Kubetzka, Discovery of Magnetic Single- and Triple- $q$  States in Mn/Re(0001), *Phys. Rev. Lett.* **124**, 227203 (2020).
- [7] S. Heinze, K. von Bergmann, M. Menzel, J. Brede, A. Kubetzka, R. Wiesendanger, G. Bihlmayer, and S. Blügel, Spontaneous atomic-scale magnetic skyrmion lattice in two dimensions, *Nat. Phys.* **7**, 713 (2011).
- [8] M. Hoffmann, J. Weischenberg, B. Dupé, F. Freimuth, P. Ferriani, Y. Mokrousov, and S. Heinze, Topological orbital magnetization and emergent hall effect of an atomic-scale spin lattice at a surface, *Phys. Rev. B* **92**, 020401(R) (2015).
- [9] K. von Bergmann, M. Menzel, A. Kubetzka, and R. Wiesendanger, Influence of the local atom configuration on a hexagonal skyrmion lattice, *Nano Lett.* **15**, 3280 (2015).
- [10] M. Takahashi, Half-filled Hubbard model at low temperature, *J. Phys. C: Solid State Phys.* **10**, 1289 (1977).
- [11] A. H. MacDonald, S. M. Girvin, and D. Yoshioka,  $\frac{t}{U}$  expansion for the Hubbard model, *Phys. Rev. B* **37**, 9753 (1988).
- [12] M. Hoffmann and S. Blügel, Systematic derivation of realistic spin models for beyond-heisenberg solids, *Phys. Rev. B* **101**, 024418 (2020).
- [13] S. Grytsiuk, J.-P. Hanke, M. Hoffmann, J. Bouaziz, O. Gomonay, G. Bihlmayer, S. Lounis, Y. Mokrousov, and S. Blügel, Topological-chiral magnetic interactions driven by emergent orbital magnetism, *Nat. Commun.* **11**, 511 (2020).
- [14] A. Lászlóffy, L. Rózsa, K. Palotás, L. Udvardi, and L. Szunyogh, Magnetic structure of monatomic Fe chains on Re(0001): Emergence of chiral multispin interactions, *Phys. Rev. B* **99**, 184430 (2019).
- [15] S. Brinker, M. dos Santos Dias, and S. Lounis, The chiral biquadratic pair interaction, *New J. Phys.* **21**, 083015 (2019).
- [16] S. Mankovsky, S. Polesya, and H. Ebert, Extension of the standard heisenberg hamiltonian to multispin exchange interactions, *Phys. Rev. B* **101**, 174401 (2020).
- [17] J.-P. Hanke, F. Freimuth, A. K. Nandy, H. Zhang, S. Blügel, and Y. Mokrousov, Role of Berry phase theory for describing orbital magnetism: From magnetic heterostructures to topological orbital ferromagnets, *Phys. Rev. B* **94**, 121114(R) (2016).
- [18] J. Bedow, E. Mascot, T. Posske, G. S. Uhrig, R. Wiesendanger, S. Rachel, and D. K. Morr, Topological superconductivity induced by a triple- $q$  magnetic structure, *Phys. Rev. B* **102**, 180504(R) (2020).
- [19] See <https://www.flapw.de>.
- [20] M. Weinert, G. Schneider, R. Podloucky, and J. Redinger, FLAPW: applications and implementations, *J. Phys.: Condens. Matter* **21**, 084201 (2009).
- [21] P. Kurz, F. Förster, L. Nordström, G. Bihlmayer, and S. Blügel, *Ab initio* treatment of noncollinear magnets with the full-potential linearized augmented plane wave method, *Phys. Rev. B* **69**, 024415 (2004).
- [22] See <https://www.vasp.at>.
- [23] G. Kresse and J. Furthmüller, Efficient iterative schemes for *ab initio* total-energy calculations using a plane-wave basis set, *Phys. Rev. B* **54**, 11169 (1996).
- [24] P. E. Blöchl, Projector augmented-wave method, *Phys. Rev. B* **50**, 17953 (1994).
- [25] G. Kresse and D. Joubert, From ultrasoft pseudopotentials to the projector augmented-wave method, *Phys. Rev. B* **59**, 1758 (1999).
- [26] See Supplemental Material at “link provided by journal” for details.
- [27] D.-P. Ji, Q. Zhu, and S.-Q. Wang, Detailed first-principles studies on surface energy and work function of hexagonal metals, *Surf. Sci.* **651**, 137 (2016).
- [28] N. M. Rosengaard and B. Johansson, Finite-temperature study of itinerant ferromagnetism in Fe, Co, and Ni, *Phys. Rev. B* **55**, 14975 (1997).
- [29] A. I. Liechtenstein, M. I. Katsnelson, V. P. Antropov, and V. A. Gubanov, Local spin density functional approach to the theory of exchange interactions in ferromagnetic metals and alloys, *J. Magn. Magn. Mat.* **67**, 65 (1987).
- [30] S. Heinze, Simulation of spin-polarized scanning tunneling microscopy images of nanoscale non-collinear magnetic structures, *Appl. Phys. A* **85**, 407 (2006).
- [31] D. Wortmann, S. Heinze, P. Kurz, G. Bihlmayer, and S. Blügel, Resolving complex atomic-scale spin structures by spin-polarized scanning tunneling microscopy, *Phys. Rev. Lett.* **86**, 4132 (2001).
- [32] K. von Bergmann, A. Kubetzka, O. Pietzsch, and R. Wiesendanger, Interface-induced chiral domain walls, spin spirals and skyrmions revealed by spin-polarized scanning tunneling microscopy, *J. Phys.: Condens. Matter* **26**, 394002 (2014).